Prediction of aerodynamic sound from circular rods via spanwise statistical modelling

D. Casalino[a],*, M. Jacob[b]

[a] Dipartimento di Ingegneria Aeronautica e Spaziale, Politecnico di Torino, Corso Duca degli Abruzzi, 24, 10129 Torino, Italy
[b] Laboratoire de Mécanique des Fluides et Acoustique, Ecole Centrale de Lyon, 36, Avenue Guy de Collongue, 69131 Ecully Cedex, France

Abstract

The Ffowcs Williams and Hawkings' acoustic analogy is combined in the time domain with a statistical model in order to take into account the three-dimensional character of the vortex shedding process from a rod in a uniform stream. By applying the model to a two-dimensional unsteady Reynolds averaged Navier–Stokes flow computation, it is shown that the three-dimensional effects, like spectral broadening around the shedding frequency, are partially recovered. The ad hoc statistical model relates a spanwise random distribution of the vortex shedding phase and wall pressure modulations to an arbitrary spanwise correlations. The phase distribution is applied to the tonal pressure signals of the computation and the resulting ad hoc signals are fed into the acoustic analogy. The study is carried out for a rod based Reynolds number of 2.2×10^4 for which the rod wake is turbulent. Numerical results compare favourably to those of an accompanying experiment.
© 2002 Elsevier Science Ltd. All rights reserved.

1. Introduction

The aerodynamic sound generated by the periodic vortex shedding from a circular cylinder is a classical problem in aeroacoustics.

The *Aeolian tones* were first investigated by Strouhal [1] in 1878 by measuring the frequency of the tonal emission from a stretched wire mounted on a hand-driven rotating apparatus. Strouhal related the sound generation to the flow friction on the wire and observed that the tonal frequency is given by $f_0 = St\, U/d$, where St is a constant, U is the velocity of the cylinder and d its diameter.

This result was confirmed in 1879 by Lord Rayleigh [2] who first observed that the Strouhal number *St* depends on the flow Reynolds number. Moreover, Rayleigh argued that, since the wire vibrates perpendicularly to the stream, the sound could not be generated by the fluid friction. Therefore, after Bénard's 1908 observation of staggered vortices in a cylinder wake and von Kármán's 1912 stability analysis of a double row of counter-rotating vortices, Rayleigh [3] related the wire tone emission and vibration to the periodic vortex shedding from the wire.

Among the several arguments in favour of Rayleigh's fatherhood of the aerodynamic sound theory[1] that related to the Aeolian tones is well established. Indeed, as early as 1896, Rayleigh [5] observed that even motionless cylinders in a fluid stream can produce a tonal emission and that the coincidence of the vortex shedding frequency with the cylinder structural frequency only increases the sound intensity.

Once the acoustic analogy theory was established by Lighthill [6] and Curle [7], Phillips [8] succeeded in predicting the Aeolian tones on the basis of some flow quantities, namely the vortex shedding frequency, the maximum lift coefficient induced by the counter-rotating vortices, and the spanwise correlation length.

The spanwise correlation length accounts for the three-dimensional character of the flow. A circular cylinder flow, in fact, remains two-dimensional up to Reynolds numbers of about 180. At higher values, three-dimensional fluctuations are imposed on the dominant vortex shedding. As a consequence, the wall pressure signals exhibit a random amplitude modulation. At very low Reynolds numbers this behaviour is presumably related [9] to a cellular structure of the vortex shedding, accompanied by *vortex dislocations* and oblique vortex shedding. At higher Reynolds numbers cellular shedding has never been observed, despite the randomly modulated behaviour of the wall pressure signals [10]. Therefore, vortex dislocations are likely to exist also at higher Reynolds numbers.

An oblique vortex shedding causes a spanwise variation of the vortex shedding phase. Furthermore, a statistical analogy exists between a random amplitude modulation and a random dispersion of the vortex shedding phase. Therefore, an ad hoc statistical model for the vortex shedding phase is described in the present paper. The model allows one to take into account, to some extent, the three-dimensional character of the flow in an acoustic analogy prediction based on a two-dimensional flow field.

The spanwise statistical method is validated on the base of Phillips' [8] Aeolian tones model, and by comparing experimental data with an acoustic analogy prediction of the sound from a $Re = 2.2 \times 10^4$ circular cylinder flow. The acoustic field is computed by applying the Ffowcs Williams and Hawkings (FW–H) acoustic analogy to aerodynamic data computed on different surfaces around the cylinder. The aerodynamic field is obtained from a two-dimensional Reynolds-averaged Navier–Stokes (RANS) computation. The same hybrid CFD/FW–H approach has been used by other authors [11–13] in order to validate the consistency of a FW–H formulation applied to a penetrable integration surface.

Once the acoustic analogy is tested, the present approach can be also used as a good benchmark for a CFD prediction, since the accuracy of the acoustic solution hinges on the accuracy of the CFD solution.

---

[1]The reader is referenced to Doak's review [4] for a suggestive dissertation on the Rayleigh's fatherhood of the aerodynamic sound theory.

2. On the three-dimensional effects in the wake of a rod

The vortex dynamics in the wake of a bluff body is of increasing concern in many engineering areas. Effects related to the intrinsic three-dimensional character of a *nominal* two-dimensional flow must be taken into account in order to predict unsteady loading, vibrations and sound generation.

The spanwise statistical model presented in this paper is concerned with the sound from a rod. It is based on Phillips' [8] intuition of a spanwise variation of the vortex shedding phase, and is inferred by recent observations of the vortex dynamics in the wake of a rod.

Different three-dimensional effects have been observed in the wake of a rod. At low Reynolds numbers, an oblique vortex shedding may occur, accompanied by discontinuities in the Strouhal–Reynolds number relationship. These effects are related to each other and are both influenced by the span end conditions, even for very high aspect ratios l/d. The Strouhal discontinuity observed by Tritton [14] near $Re = 75$ is caused by a transition from one oblique shedding mode to another one [9]. This transition can be explained by a change in the shedding pattern from one where the central flow is able to match the end conditions to one where the central flow is unable to match the end conditions and generates a cell of higher shedding frequency. Up to three coexisting frequency cells have been observed [15]. At the interface between two cells *vortex dislocations* occur during periods in which vortices move out of phase with each other. The coexistence of cells of different frequency results in a low-frequency quasi-periodic amplitude modulation of the fluctuating quantities in the near wake. Furthermore, at the boundary between two cells, abrupt phase jumps can take place at the amplitude modulation frequency.

The main three-dimensional effect observed at higher Reynolds numbers is a spanwise variation of the vortex shedding phase, accompanied by a random amplitude modulation of the fluctuating quantities in the near wake of the rod. Since the vortex shedding is not in phase along the rod span, spanwise pressure gradients take place, which induce spanwise velocity fluctuations. Near the end plates the spanwise component of the fluctuating velocity vanishes, leading to an enhancement of the vortex shedding uniformity. Experiments conducted by Szepessy and Bearman [10] in the high-Reynolds number range 1×10^4–1.3×10^5 show that a weak shedding mode reappears somewhat periodically at about 10–20 times the Strouhal period, and has a duration of about 3–7 shedding periods. Szepessy and Bearman also observed a phase shift between a wall pressure signal in the rod mid-plane and a velocity signal near the rod, both taken $90°$ away from the flow direction. The phase shift increased with the separation distances between the two transducers. Despite the amplitude modulation, no cellular vortex shedding was observed.

3. Experimental investigation

An experiment is carried out in the small anechoic room of the Ecole Centrale de Lyon (6 m × 5 m × 4 m), where air is supplied by a low-speed subsonic anechoic wind tunnel.

The reference configuration is a $d = 0.016$ m rod extending by $l = 0.3$ m in the span direction. The rod is fixed between two parallel rectangular plates and is placed into the potential core of a partially flanged rectangular jet. The inflow velocity is $V_\infty = 20$ m/s, corresponding to $M_\infty = 0.06$ and $Re = 2.2 \times 10^4$. The experimental set-up is sketched in Fig. 1.

Acoustic measurements are taken at a distance $r = 1.38$ m from the rod mid-point, at various observation angles in the mid-span plane. A Brüel and Kjäer type 4191 microphone with a Brüel & Kjäer type 2669 preamplifier is used for these measurements. Data acquisitions are carried out with a spectral resolution of 2 Hz, from 0 to 6400 Hz, and the number of averages is 400. The Brüel & Kjäer software *Pulse* is used for the signal acquisition and processing.

Measurements of wall pressure fluctuations were performed in order to investigate the statistical behaviour of the vortical flow in the wake of the rod. The experimental arrangement is sketched in Fig. 2. The rod is constituted of two parts. One part is fixed, the other can rotate around the rod axis. Six pressure pinholes are drilled on the rod: one on the movable section, the
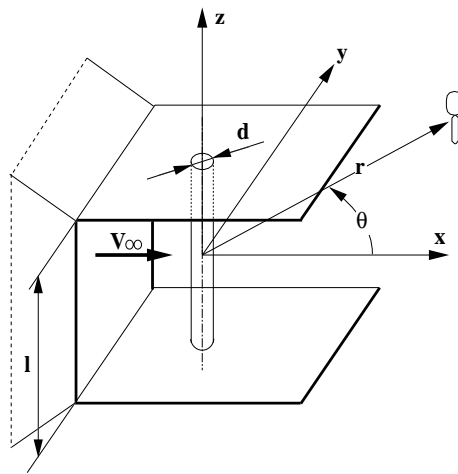
Fig. 1. Experimental set-up.
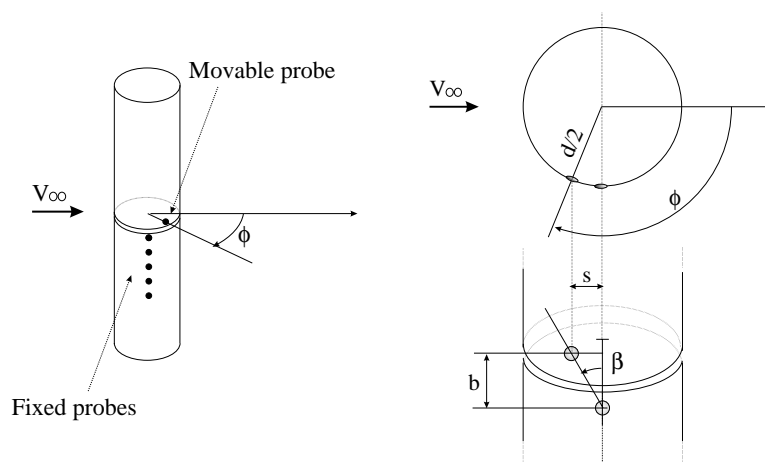
Fig. 2. Rod configuration. Pressure pinholes of 0.5 mm diameter are drilled on the rod surface and communicate with external condenser microphones. Five probes are on the fixed section, whereas only one probe is on the movable section. The distance between the movable probe and the fixed one closest to the mid-span section is $b = 2$ mm.

others on the fixed one. The fixed probes are located $90°$ away from the streamwise direction. The pinholes communicate with external condenser microphones through capillary tubes [16]. Hence, two-point coherence and correlation measurements can be performed with both angular and spanwise spacing.

3.1. Acoustic measurements

In Fig. 3 the acoustic power spectral density measured around the rod is plotted.

Aeolian tones are detected at each observation angle, as revealed by the prominent peak at the frequency $f_0 = 250$ Hz, corresponding to a typical Strouhal number of 0.2.

Both the Strouhal peak and the second harmonic peak at $f = 3f_0$ are generated by the unsteady lift induced on the rod by the Kármán vortex street. A first harmonic peak at $f = 2f_0$ arises away from the azimuthal position $\theta = 90°$ and increases towards $\theta = 0$. This peak is related to the unsteady drag induced on the rod.

All the peaks exhibit a significant broadening around the harmonic frequencies. Such a behaviour is of main concern in the present work and is presumably due to the three-dimensional nature of the vortex shedding process. As previously discussed, pressure fluctuations on the rod surface undergo a randomly modulated quasi-periodic behaviour. A similar behaviour is thus expected in the far pressure field, resulting in broadened harmonic peaks.

In Fig. 3(a) the rod sound is compared to the noise from the jet alone. At frequencies higher than about 2000 Hz the rod spectrum is likely to be contaminated by the background noise.

3.2. Wall pressure measurements

In Fig. 4 the coherence at the Strouhal frequency and the correlation coefficient are plotted. Both these quantities are defined in Appendix A. The reference probe is at $\eta_d = 0$, η_d denoting the distance from the mid-span plane made dimensionless by the rod diameter. Data are fitted by a Gaussian $\exp(-\eta_d^2/2L_g^2)$ function, with $L_g = 4.7$ for the coherence function, and $L_g = 6.6$ for the correlation coefficient. The vortex shedding process is therefore correlated upon a distance of about $6.5d$.

Cross-spectrum measurements of the fluctuating pressure are also made between a fixed reference probe at $90°$ away from the streamwise direction and probes at different angular positions ϕ, with an angular step of $5°$.

As shown in Fig. 5(a), the cross-spectrum peaks when the movable probe is at $\phi = 100°$. This experimental inaccuracy can be indeed justified to some extent. As sketched in Fig. 2(b), a circumferential skew s between the fixed and the closest movable probe results in the skew angle $\beta \simeq \tan^{-1}[d\sin(\phi - \pi/2)/2b]$, where $b = 2 \times 10^{-3}$ m is the spanwise distance between the fixed and the movable probe. In other words, the angle β measures the deviation of the movable probe from the vertical axis cutting through the fixed probes. A skew angle $\beta = 35°$ corresponds to $\phi = 100°$. Fig. 5 shows that also the coherence at the Strouhal frequency is maximum when the movable probe is at $\phi = 100°$, but it is almost maximal over a wide range of angles. Hence, $\beta \simeq 35°$ could be interpreted as a time-averaged vortex shedding angle. This discussion is quite far from being a quantitative analysis of the three-dimensional effects in the wake of a rod. The phenomenology is indeed intrinsically complex and not completely understood at present time. Nevertheless,
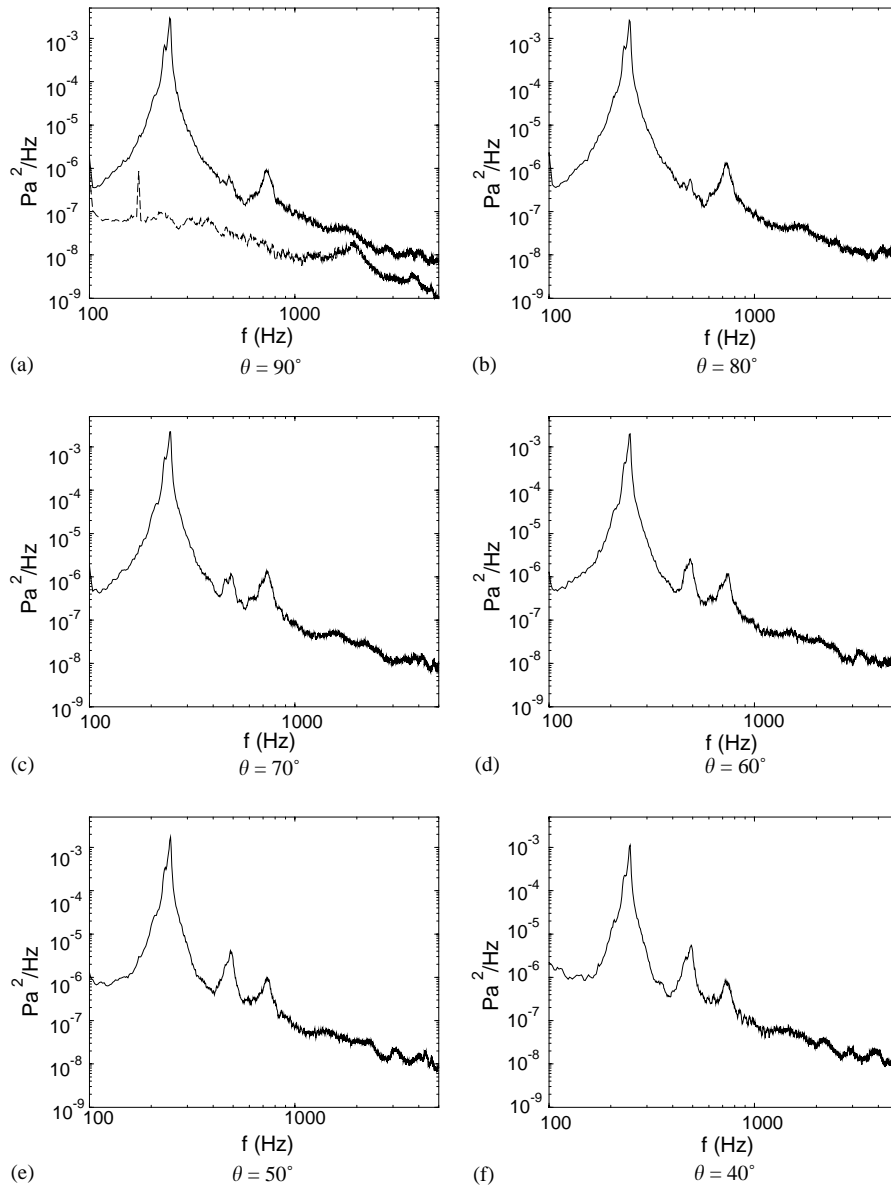
Fig. 3. Power spectral density of the rod noise at different observation angles. Comparison with the jet-alone noise at $\theta = 90°$.

measurements such as those described in this paper may be used to investigate the three-dimensional vortex dynamics in the wake of a rod.

In Fig. 5 the angular coherence at the Strouhal frequency and its peaks at the first and second harmonics are plotted against the angular position of the movable probe. At the Strouhal frequency the coherence is almost one from $\phi \simeq 60°$ to $\phi \simeq 120°$, the maximum being

reached when the movable probe is at about $\phi = 100°$. Conversely, at higher harmonics, the coherence is maximum when the movable probe is at $\phi = 90°$. Surprisingly, the first harmonic peak of coherence reaches a local minimum at $\phi = 100°$, where the Strouhal peak is maximum.

The wall pressure signals corresponding to the maximum cross-spectrum amplitude are plotted in Fig. 6. Interestingly, weak amplitude cycles reappear somewhat periodically at about 15–20 times the Strouhal period, and have a duration of about 4–5 shedding periods.

Finally, in Fig. 7 the wall pressure signals taken at $\phi = 90°$ along the rod span are plotted. Both a phase shift between signals and sporadic phase jumps can be noticed. A similar behaviour was observed by Szepessy and Bearman [10] in the Reynolds number range 1×10^4–1.3×10^5.

In this section some effects related to the three-dimensional character of a circular cylinder flow have been described. The spanwise loss of coherence, the wall pressure random amplitude modulation, and the phase shift between signals at different spanwise locations give evidence of the three-dimensional structure of the wake behind the rod.
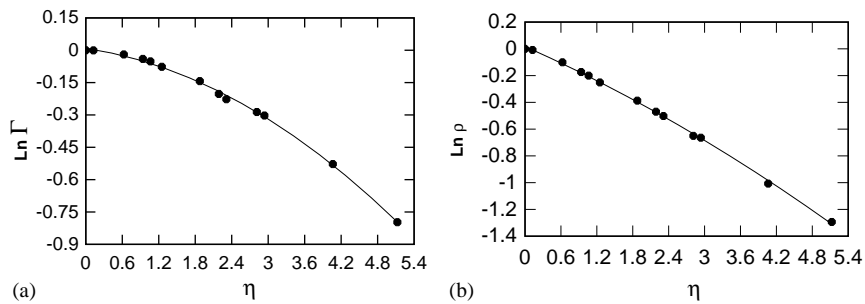
Fig. 4. Spanwise coherence and correlation coefficient on the rod surface at $\phi = 90°$ (logarithmic scale). (a) Coherence function $\ln(\Gamma)$; (b) correlation coefficient $\ln(\rho)$. (●●) Experimental data; (——) Gaussian interpolation.
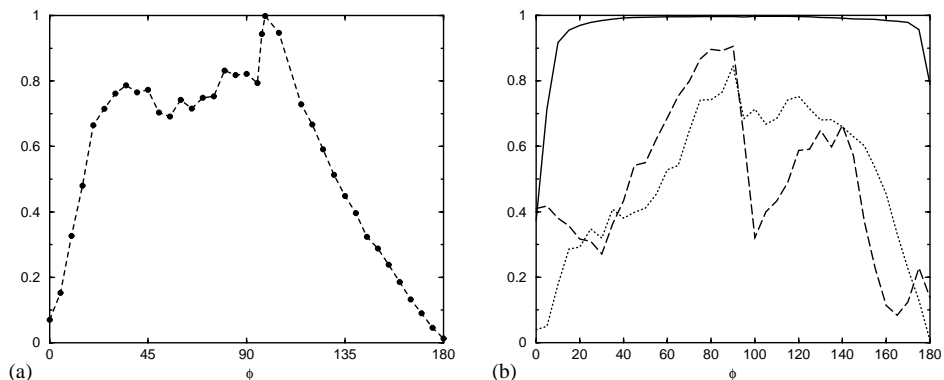
Fig. 5. Cross-spectrum and coherence measurements between a reference pressure probe at $\phi = 90°$ and probes at different ϕ. (a) $|S_{12}/\max(|S_{12}|)|$ at the Strouhal frequency f_0; (b) maximum values of Γ at the Strouhal frequency f_0 and higher harmonics. —— f_0, — — $2f_0$, - - - - $3f_0$.
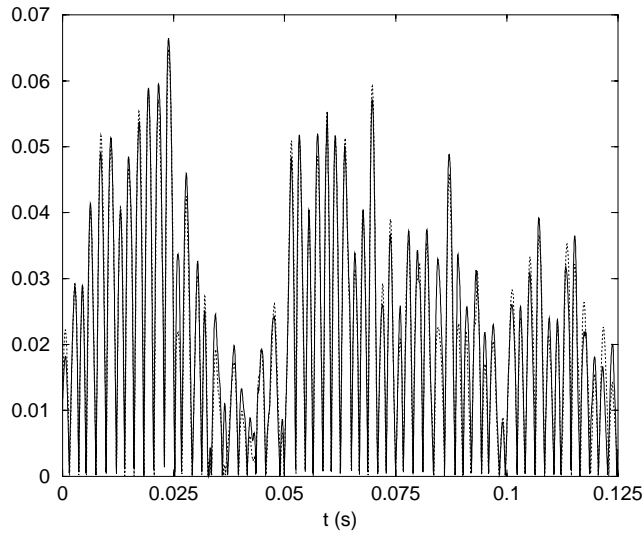
Fig. 6. Wall pressure signals: (——) movable probe at $\phi = 100°$; (- - - -) fixed probe.
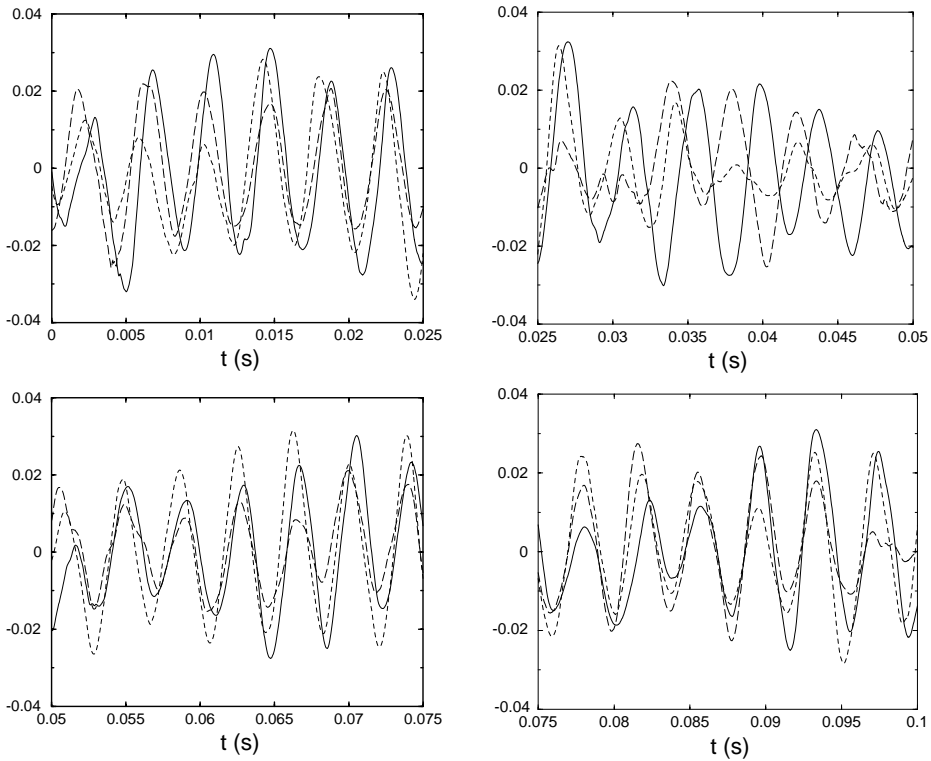
Fig. 7. Wall pressure signals at different spanwise positions: (——) $\eta_d = 0.125$; (- - - -) $\eta_d = 2.437$; (— —) $\eta_d = 5.250$. Pressure probes at $\phi = 90°$.

4. Aerodynamic computation

The compressible finite volume RANS code *Proust* [17] is used in the current investigation. Both the convective fluxes and the viscous terms are evaluated by using a second order centred scheme. The solution is advanced in time by using an explicit second order scheme based on a five-step Runge–Kutta factorization.

Non-reflecting boundary conditions and grid stretching in the outer domains are used in order to reduce spurious reflections of acoustic waves.

The turbulence model used is the two-equations Wilcox [18] k–ω model, where k is the turbulent kinetic energy and ω is related to the turbulent dissipation. The inflow conditions and the flow parameters are $\rho_\infty = 1.225$ kg/m^3, $V_\infty = 20$ m/s, $p_\infty = 101\,253.6$ Pa and $\mu_\infty = 1.78 \times 10^{-5}$ kg/m s. The turbulent kinetic energy has a uniform initial value of 0.01 as measured in experiments. The inflow boundary conditions remain the same throughout the computation.

An approximated steady potential flow is used as initial solution. Furthermore, a strong line-vortex in proximity of one separation point on the cylinder is added to the initial field in order to induce a vortex shedding as soon as the computation is started, and thus to accelerate the convergence to a periodic flow.

The computational mesh is based on 197×193 points. It is circumferentially clustered in the wake region. The minimum circumferential spacing, at the rod base point ($\phi = 0°$), is $2.5 \times 10^{-3}d$, and the thickness of the mesh wall layer is $5 \times 10^{-4}d$.

The computational time-step is 6.25×10^{-8} s, corresponding to about 5×10^5 iterations per aerodynamic cycle. 2048 aerodynamic fields are stored for the acoustic computation, covering 8.04×10^{-2} s.

5. Acoustic computation

The rotor noise code *Advantia* [19] is used for the acoustic prediction. For the purposes of the present investigation, only surface integrals are computed, since at low Mach numbers, the volume sources give a vanishing contribution to the acoustic radiation. The consistency of this approximation is checked by comparing acoustic results obtained from different integration surfaces.

For the sake of the present work *Advantia* exploits the retarded time penetrable FW–H formulation proposed by Brentner and Farassat [20].

By setting a reference length l_{ref}, a reference velocity U_{ref}, a reference time l_{ref}/U_{ref} and a reference dynamic pressure p_d the thickness and loading noise expressions in Ref. [19] take the form

$$
\frac{2\pi}{p_d} p'_Q(\mathbf{X}, \theta)
$$

$$
= \int_{f=0} \left[\frac{\dot{V}_i \hat{n}_i + \dot{q}_i \hat{n}_i + (V_i + q_i)\dot{\hat{n}}_i}{R(1 - M_r)^2} + \frac{(V_n + q_n)\{R\dot{M}_r + (M_r - M^2)/M_{ref}\}}{R^2(1 - M_r)^3} \right]_{ret} dS
$$

$$
- \int_{f=0} \left[M_{or} \frac{\dot{V}_i \hat{n}_i + \dot{q}_i \hat{n}_i + (V_i + q_i)\dot{\hat{n}}_i}{R(1 - M_r)^2} \right]_{ret} dS
$$

$$- \int_{f=0} \left[\frac{M_{or} \dot{M}_r (V_i + q_i)\hat{n}_i}{R(1 - M_r)^3} \right]_{ret} \mathrm{d}S$$

$$- \int_{f=0} \left[\frac{\{2M_{or}M_r - M_{or}M^2 - M_{oi}M_i(1 - M_r) - M_{or}M_r^2\}(V_i + q_i)\hat{n}_i}{M_{ref} R^2 (1 - M_r)^3} \right]_{ret} \mathrm{d}S$$

$$- \int_{f=0} \left[\frac{(V_i + q_i)\hat{n}_i M_{or}}{M_{ref} R^2 (1 - M_r)} \right]_{ret} \mathrm{d}S, \tag{1}$$

$$\frac{2\pi}{p_d} p_L'(\mathbf{X}, \theta) = \int_{f=0} \left[\frac{M_{ref}\chi_r}{R(1 - M_r)^2} \right]_{ret} \mathrm{d}S + \int_{f=0} \left[\frac{\lambda_r - \lambda_M}{R^2(1 - M_r)^2} \right]_{ret} \mathrm{d}S$$

$$+ \int_{f=0} \left[\frac{M_{ref}\lambda_r \{R\dot{M}_r + (M_r - M^2)/M_{ref}\}}{R^2(1 - M_r)^3} \right]_{ret} \mathrm{d}S. \tag{2}$$

Both the observer $\mathbf{X}$ and the integration surface $f = 0$ move at the constant velocity $c\mathbf{M}_o = -V_\infty \hat{\mathbf{i}}$ and the flow at infinity is at rest. Dots on quantities denote time derivatives with respect to the dimensionless source time. Square brackets enclose quantities evaluated at the retarded time θ_{ret} obtained from the dimensionless retarded time equation

$$\theta_{ret} = \theta - (\mathbf{X}(\theta) - \mathbf{Y}(\theta_{ret}))M_{ref}, \tag{3}$$

where $\mathbf{Y}(\theta_{ret})$ is a source point on the integration surface at the retarded time θ_{ret}. Quantities in Eqs. (1) and (2) are all described in Appendix B.

2048 aerodynamic fields are used for the acoustic computation (about 24 vortex shedding cycles, $t_{end} = 8.04 \times 10^{-2}$ s and $\Delta f = 12.19$ Hz). The observation distance from the airfoil mid point is $r = 1.38$ m ($kr = 6.37$ for a typical Strouhal number $St = 0.2$). Integrations are performed upon the cylinder surface and upon penetrable surfaces around the cylinder. The aerodynamic field on both physical and penetrable surfaces is extracted directly from the CFD solution and a Gaussian quadrature is used to compute the surface integrals. The rod span is discretized by 20 equal segments.

In order to deal with truncated time series, data are multiplied by the Tukey weighting function $w(t) = 0.815[1 - \cos(2\pi t/t_{end})]$ before performing Fourier analyses. The energy of the original signals is preserved by scaling the windowed data.

6. The spanwise statistical model

At Reynolds numbers higher than about 180 the flow past a circular cylinder is three-dimensional. This causes the wall pressure fluctuations to exhibit a modulated behaviour. The quasi-periodic amplitude modulation observed at low Reynolds numbers is related [9] to a cellular structure of the vortex shedding. Spanwise inhomogeneities such as boundary layers upon the end plates,[2] non-uniform inflow conditions or a spanwise-varying diameter induce the formation of *cells*, i.e. regions of constant shedding frequency along the rod span. At the interface between two cells an abrupt frequency jump occurs. The interaction between two neighbouring cells of

---

[2] The end conditions affect the vortex shedding over the entire rod span, even for aspect ratio of the order of 100.

frequency f_a and f_b, respectively, induces a beat behaviour at the frequency $|f_a - f_b|$. When the vortices in two adjacent cells are nearly in phase, their mutual interference generates an oblique vortex shedding. Conversely, when two cells are out of phase, a contorted vortical structure, say *vortex dislocation*, is produced. Hence, oblique shedding, vortex dislocation and cellular shedding are different aspects of the same phenomenology. At higher Reynolds number random amplitude modulations have been observed [10], accompanied by spanwise phase shift and jumps along the rod span.

Both an oblique vortex shedding and a random amplitude modulation can be related to a random variation of the vortex shedding phase. Therefore, an ad hoc spanwise statistical model is first developed on the base of Phillips' [8] model and successively applied to the rod noise prediction.

6.1. Phillips' model

Consider a motionless rod of diameter d and span l in a fluid stream with velocity V_∞. Set $l_{ref} = d$ and $U_{ref} = V_\infty$ in Eqs. (1) and (2). Consider a fixed observation point $r_0 d(\cos\theta, \sin\theta, 0)$, r_0 being the dimensionless observation distance from the rod mid-point and θ the angle away from the streamwise direction.

In the geometrical ($r_0 \gg 1$) and acoustical ($M_\infty r_0 2\pi St \gg 1$) farfield limits, provided that an integration upon the rod surface is made, Eqs. (1) and (2) reduce to

$$p'(r_0, \theta, \tau) = \frac{p_d M_\infty r_0 \sin\theta}{4\pi} \int_{-l/2d}^{l/2d} \frac{\mathrm{d}\eta_d}{R^2(1 + M_\infty r_0 \cos\theta / R)^2} \hat{r}_i \int_{\mathscr{L}} [\dot{C}_p]\hat{n}_i \, \mathrm{d}l, \tag{4}$$

where $p_d = \rho_\infty V_\infty^2 / 2$ is the free-stream dynamic pressure and $R = \sqrt{r_0^2 + \eta_d^2}$ is the dimensionless distance between the observer and a point source on the rod, with η_d denoting the dimensionless spanwise co-ordinate. The time derivative of the pressure coefficient is evaluated at the dimensionless retarded time

$$\tau_{ret} = \tau - R M_\infty. \tag{5}$$

Supposing an observer sufficiently far from the rod, such that $r_0 \gg l/2d$, yields

$$p'(r_0, \theta, \tau) = \frac{p_d M_\infty}{4\pi r_0 (1 + M_\infty \cos\theta)^2} \int_{-l/2d}^{l/2d} \mathrm{d}\eta_d \, \hat{r}_i \int_{\mathscr{L}} [\dot{C}_p]\hat{n}_i \, \mathrm{d}l. \tag{6}$$

Finally, neglecting the unsteady drag component by substituting

$$\int_{\mathscr{L}} [\dot{C}_p]\hat{n}_i \, \mathrm{d}l \simeq -[\dot{C}_l]\hat{j} \tag{7}$$

into Eq. (6) leads to the *compact dipole* Aeolian tones radiation

$$p'(r_0, \theta, \tau) = \frac{-p_d M_\infty \sin\theta}{4\pi r_0 (1 + M_\infty \cos\theta)^2} \int_{-l/2d}^{l/2d} [\dot{C}_l] \, \mathrm{d}\eta_d. \tag{8}$$

Although the vortex-induced fluctuating lift may be of the same amplitude along the rod span, the phase of the lift may vary stochastically as $\tilde{\varphi}(\eta_d)$. Thus, following Phillips [8], the fluctuating lift coefficient can be written as

$$C_l(\eta_d, \tau) = C_{l\,max} \exp\{-\mathrm{i}(2\pi St \tau + \tilde{\varphi}(\eta_d))\}. \tag{9}$$

Substituting Eq. (9) into Eq. (8) yields

$$p'(r_0, \theta, \tau) = \frac{\mathrm{i}p_d M_\infty \, St \, C_{l\,max} \, l \sin\theta}{2r_0 d(1 + M_\infty \cos\theta)^2} \mathrm{e}^{-\mathrm{i}[2\pi \, St \, (\tau - M_\infty r_0)]} \int_{-1/2}^{+1/2} \mathrm{e}^{-\mathrm{i}\tilde{\varphi}(\eta)} \, \mathrm{d}\eta, \tag{10}$$

where η is the spanwise co-ordinate made dimensionless by the rod span. Hence, the acoustic intensity is given by

$$I = I_{det} \int_{-1/2}^{+1/2} \int_{-1/2}^{+1/2} \exp\{-\mathrm{i}(\tilde{\varphi}(\eta_1) - \tilde{\varphi}(\eta_2))\} \, \mathrm{d}\eta_1 \, \mathrm{d}\eta_2, \tag{11}$$

where

$$I_{det} = \frac{\rho_\infty V_\infty^6 C_{l\,max}^2 \, St^2 \, l^2 \sin^2\theta}{32 c_0^3 r_0^2 d^2 (1 + M_\infty \cos\theta)^4} \tag{12}$$

denotes the farfield sound intensity of a deterministic flow (fully correlated along the rod span). If the correlation length is small compared to the rod span, the double integral in Eq. (11) can be approximated as

$$\int_{-1/2}^{+1/2} \int_{-1/2}^{+1/2} \exp\{-\mathrm{i}(\tilde{\varphi}(\eta_1) - \tilde{\varphi}(\eta_2))\} \, \mathrm{d}\eta_1 \, \mathrm{d}\eta_2 \simeq \int_{-\infty}^{+\infty} \rho(\eta) \, \mathrm{d}\eta, \tag{13}$$

where the correlation coefficient $\rho(\eta) = \int_{-1/2}^{+1/2} \exp\{-\mathrm{i}(\tilde{\varphi}(\eta_1) - \tilde{\varphi}(\eta_1 + \eta))\} \, \mathrm{d}\eta_1$ can be *reasonably* supposed to be Gaussian or Laplacian. In the first case it results that

$$\rho(\eta) = \exp\left(-\frac{\eta^2}{2L_g^2}\right) \quad \text{and} \quad I = I_{det}\sqrt{2\pi}L_g, \tag{14}$$

whereas in the second case

$$\rho(\eta) = \exp\left(-\frac{|\eta|}{L_l}\right) \quad \text{and} \quad I = I_{det}2L_l. \tag{15}$$

6.2. The method of the phase variance distribution

The fluctuating pressure on the rod surface at $90°$ away from the streamwise direction is representative of the fluctuating lift. Thus, for two spanwise locations one can write $p_1(t) = P\cos(2\pi f_0 t + \tilde{\varphi}_1)$ and $p_2(t) = P\cos(2\pi f_0 t + \tilde{\varphi}_2)$. The related cross-correlation function is given by

$$\begin{aligned}
C_{12}(\Theta) &= \mathscr{E}[p_1(t)p_2(t + \Theta)] \\
&= \frac{P^2}{2}\,\mathscr{E}[\cos\tilde{\varphi}_1\cos\tilde{\varphi}_2]\cos(2\pi f_0\Theta) - \frac{P^2}{2}\,\mathscr{E}[\cos\tilde{\varphi}_1\sin\tilde{\varphi}_2]\sin(2\pi f_0\Theta) \\
&\quad + \frac{P^2}{2}\,\mathscr{E}[\sin\tilde{\varphi}_1\cos\tilde{\varphi}_2]\sin(2\pi f_0\Theta) + \frac{P^2}{2}\,\mathscr{E}[\sin\tilde{\varphi}_1\sin\tilde{\varphi}_2]\cos(2\pi f_0\Theta),
\end{aligned} \tag{16}$$

where $\mathscr{E}[\,]$ denotes the expected value.

Taking the first point in $\eta = 0$ and setting $\tilde{\varphi}_2 = \tilde{\varphi}$, reduces Eq. (16) to

$$C_{12}(\Theta) = \frac{P^2}{2}\mathscr{E}[\cos\tilde{\varphi}]\cos(2\pi f_0\Theta) - \frac{P^2}{2}\mathscr{E}[\sin\tilde{\varphi}]\sin(2\pi f_0\Theta). \qquad (17)$$

This is equivalent to supposing that the flow is statistically homogenous along the rod span and that the random phase $\tilde{\varphi}$ denotes indeed a random phase shift. The corresponding spanwise correlation coefficient is given by

$$\rho(\eta) \equiv C_{12}(0) = \mathscr{E}[\cos\tilde{\varphi}] \qquad (18)$$

whereas the coherence function is given by

$$\Gamma(\eta,f) = \frac{|S_{12}(\eta,f)|}{\sqrt{S_{11}}\sqrt{S_{22}}} = \mathscr{E}[\cos\tilde{\varphi}]\delta(f - f_0) - \mathscr{E}[\sin\tilde{\varphi}]\delta(f - f_0), \qquad (19)$$

where the cross-spectrum S_{12} is the Fourier transform of the cross-correlation function given in Eq. (17).

Random phase shifts may occur for different and independent causes: inflow non-uniformity, surface roughness, etc. According to the *central limit theorem*, this is sufficient to suppose that the random variable $\tilde{\varphi}$ has a Gaussian probability density. Physically this corresponds to a condition of maximum entropy, namely, the less *structured* or deterministic condition. In the present case, it is assumed that random perturbations from the incoming and surrounding turbulent flow (the rod is located in the potential core of a jet) are mainly responsible for the spanwise coherence loss of the deterministic shedding. Hence, not the shedding itself, but its deviation from periodicity is directly related to the surrounding turbulence and can thus be modelled by a Gaussian probability.

Hence, assume a spanwise phase distribution with a Gaussian probability density $\mathscr{P}$, whose variance w is zero on the rod mid-span plane ($\eta = 0$) and increases symmetrically towards the rod extremities ($\eta = \pm 1/2$), i.e.,

$$\mathscr{P}(\tilde{\varphi},\eta) = \frac{\exp(-\tilde{\varphi}^2/(2w(\eta)))}{\sqrt{2\pi w(\eta)}}. \qquad (20)$$

Clearly, a spanwisely increasing variance accounts for the intrinsic phase shift nature of $\tilde{\varphi}$. Two methods are described below to determine the value of ρ and Γ.

If $\tilde{x}$ denotes a random variable with probability density $\mathscr{P}(\tilde{x})$, the expected value of a generic function $f(\tilde{x})$ is given by $\mathscr{E}[f(\tilde{x})] = \int_{-\infty}^{+\infty} f(\tilde{x})\mathscr{P}(\tilde{x})\,d\tilde{x}$. Thus, applying this fundamental property to Eq. (19) leads to

$$\mathscr{E}[\sin\tilde{\varphi}] = \int_{-\infty}^{+\infty} \sin\tilde{\varphi}\,\frac{\exp(-\tilde{\varphi}^2/(2w))}{\sqrt{2\pi w}}\,d\tilde{\varphi} = 0 \qquad (21)$$

and

$$\mathscr{E}[\cos\tilde{\varphi}] = \int_{-\infty}^{+\infty} \cos\tilde{\varphi}\,\frac{\exp(-\tilde{\varphi}^2/(2w))}{\sqrt{2\pi w}}\,d\tilde{\varphi} = \exp\left(-\frac{w}{2}\right), \qquad (22)$$

where use of the known integral $\int_{-\infty}^{+\infty} \cos(bx)\exp[-ax^2]\,dx = \sqrt{(\pi/a)}\exp(-b^2/(4a))$ has been made. Therefore, when $\tilde{\varphi}$ is a random variable with a symmetric probability density, the

coherence function can be also interpreted as the correlation coefficient, i.e.,

$$\Gamma(\eta, f) = \rho(\eta)\delta(f - f_0). \tag{23}$$

Another method for evaluating $\mathscr{E}[\cos \tilde{\varphi}]$ is to consider the Taylor series of $\cos \tilde{\varphi}$, writing

$$\mathscr{E}[\cos \tilde{\varphi}] = \mathscr{E}\left[\sum_{n=0}^{\infty} \frac{(-1)^n}{(2n)!} \tilde{\varphi}^{2n}\right] = \sum_{n=0}^{\infty} \frac{(-1)^n}{(2n)!} \mathscr{E}[\tilde{\varphi}^{2n}]. \tag{24}$$

Since $\tilde{\varphi}$ has a Gaussian density probability, it results that

$$\mathscr{E}[\tilde{\varphi}^0] = 1 \quad \text{and, for } n \geqslant 1,$$
$$\mathscr{E}[\tilde{\varphi}^{2n-1}] = 0$$
$$\mathscr{E}[\tilde{\varphi}^{2n}] = (2n - 1)(2n - 3) \cdot \cdots \cdot 3 \cdot 1 \cdot w^n.$$

Thus, substituting into Eq. (24) and performing some algebra, i.e.,

$$\begin{aligned} \mathscr{E}[\cos \tilde{\varphi}] &= \sum_{n=0}^{\infty} \frac{(-1)^n}{(2n)!} (2n - 1)(2n - 3) \cdot \cdots \cdot 3 \cdot 1 \cdot w^n \\ &= \sum_{n=0}^{\infty} \frac{(-w)^n}{2n(2n - 2)(2n - 4) \cdot \cdots \cdot 4 \cdot 2} \\ &= \sum_{n=0}^{\infty} \frac{(-w/2)^n}{n(n - 1)(n - 2) \cdot \cdots \cdot 3 \cdot 1} \\ &= \sum_{n=0}^{\infty} \frac{1}{n!}\left(-\frac{w}{2}\right)^n = \exp\left(-\frac{w}{2}\right) \end{aligned} \tag{25}$$

the same result as in Eq. (22) is obtained.

Concluding, the spanwise correlation coefficient at $\phi = 90°$ on the rod surface takes the form

$$\rho(\eta) = \exp\left(-\frac{w}{2}\right). \tag{26}$$

Two variance distributions are considered as demonstrative examples, leading to a Gaussian and a Laplacian correlation coefficient, respectively. These are

(a) a quadratic variance distribution

$$w(\eta) = 4w_{max}\eta^2 \tag{27}$$

yielding

$$\rho(\eta) = \exp\left(-\frac{\eta^2}{2L_g^2}\right) \tag{28}$$

with

$$w_{max} = (2L_g)^{-2}; \tag{29}$$

(b) a linear variance distribution

$$w(\eta) = 2w_{max}|\eta| \tag{30}$$

yielding

$$\rho(\eta) = \exp\left(-\frac{|\eta|}{L_l}\right) \tag{31}$$

with

$$w_{max} = L_l^{-1}. \tag{32}$$

Here L_g and L_l denote the Gaussian and Laplacian correlation lengths, respectively, made dimensionless by the rod span.

The correlation coefficients obtained from a quadratic and a linear spanwise variance of the phase, respectively, are plotted in Fig. 8. Numerical values, obtained from a randomly generated Gaussian distribution of $\tilde{\varphi}$, are compared with the Gaussian and Laplacian functions of the span spacing η.

By assuming a lift coefficient with the same phase distributions used to plot the correlation coefficients in Fig. 8, Eq. (4) provides the acoustic radiation plotted in Fig. 9. Interestingly, an amplitude modulation can be observed in the acoustic signals, resulting in a spectral broadening around the Strouhal peak.

In Fig. 10(a) the acoustic intensity obtained from Eq. (11) by assuming a Gaussian and a Laplacian correlation coefficient, as in Eqs. (14) and (15), respectively, are compared to the acoustic intensity obtained from Eq. (4) with a Gaussian distribution of the lift phase $\tilde{\varphi}$ along the rod span. Deviations from Phillips' prediction are only due to the fact that the rod has been supposed to be finite for the numerical integration of Eq. (4). Thus, erroneous predictions can be made if the Phillips' model is applied to "short" rods. In this case, in fact, the approximation (13) is not consistent.

6.3. Random amplitude modulation versus spanwise phase dispersion

The random amplitude modulation observed at high Reynolds numbers can be described as

$$p(t) = \frac{P}{2}[\cos(2\pi f_0 t) + \cos(2\pi \tilde{f}_m t)], \tag{33}$$
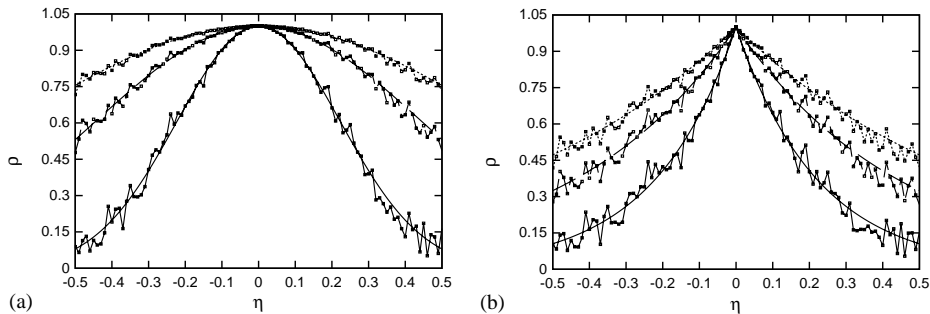
Fig. 8. Correlation coefficients resulting from random phase distributions with a quadratic (27) and a linear (30) spanwise variance of the vortex shedding phase. Lengths are made dimensionless by the rod span. (a) Gaussian correlation coefficient. Comparison between the analytical expression (28) and numerical values obtained by means of the quadratic variance distribution (29). —— $L_g = 0.222$, — — $L_g = 0.444$, - - - - $L_g = 0.666$. (b) Laplacian correlation coefficient. Comparison between the analytical expression (31) and numerical values obtained by means of the linear variance distribution (32). —— $L_l = 0.222$, — — $L_l = 0.444$, - - - - $L_l = 0.666$.
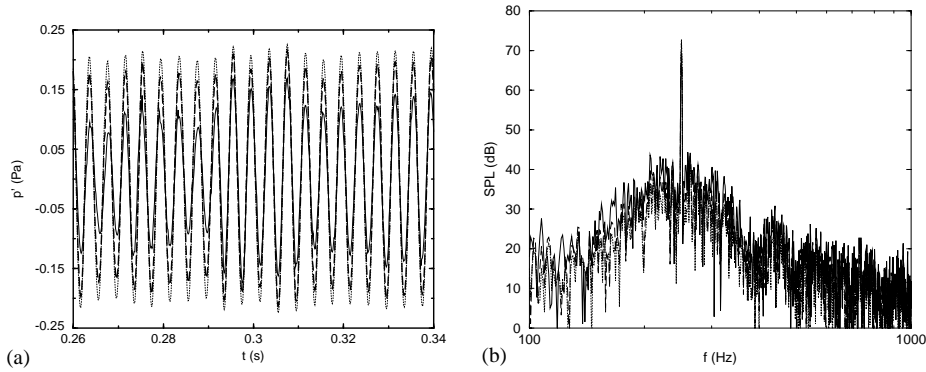
Fig. 9. Sound from a compact rod at a distance $r_0 = 138$ and an observation angle $\theta = 90°$, obtained by forcing a Gaussian correlation coefficient into Eq. (4): (——) $L_g = 0.222$; (— · —) $L_g = 0.444$; (- - - -) $L_g = 0.666$. The values $d = 0.016$ m, $l = 0.3$ m, $V_\infty = 20$ m/s, $C_{l\,max} = 0.75$, $r_0 = 138$ and $\theta = 90°$ have been used in the computation. (a) Time trace of the acoustic pressure; (b) spectrum of the acoustic pressure.
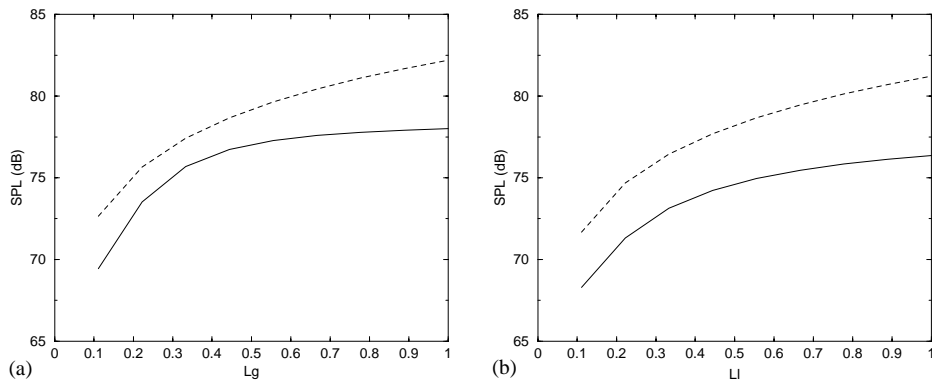
Fig. 10. Sound intensity from a rod for different values of the correlation length. Comparison between Phillips' analytical results and the compact dipole formulation (4), with a randomly generated spanwise phase distribution of the unsteady lift coefficient. (a) Gaussian spanwise correlation coefficient; (b) Laplacian spanwise correlation coefficient (——) Compact dipole formulation; (- - - -) Phillips' model.

where $\tilde{f}_m$ denotes a random frequency which differs from f_0 only slightly. Upon setting $\tilde{f}_b = f_0 - \tilde{f}_m$, $\tilde{f}_b$ being the random beat frequency ($\tilde{f}_b \ll f_0$), Eq. (33) yields

$$p(t) = P\cos\left\{2\pi\left(f_0 - \frac{\tilde{f}_b}{2}\right)t\right\}\cos\left(2\pi\frac{\tilde{f}_b}{2}t\right) \simeq P\cos(2\pi f_0 t)\cos(\pi\tilde{f}_b t). \qquad (34)$$

At two different spanwise positions the pressure signals are

$$p_1(t) = P\cos(2\pi f_0 t)\cos(\pi\tilde{f}_{b1}t), \quad p_2(t) = P\cos(2\pi f_0 t)\cos(\pi\tilde{f}_{b2}t). \qquad (35)$$

The resulting correlation coefficient is given by

$$\rho(\eta) = \mathscr{E}[\cos\{\pi(\tilde{f}_{b1} - \tilde{f}_{b2})t\}]. \tag{36}$$

This expression coincides with that given in Eq. (18) if the random quantity $\pi(\tilde{f}_{b1} - \tilde{f}_{b2})t$ is interpreted as a random phase $\tilde{\varphi}$. This holds if the random process is ergodic, which is the case of the flow considered in the present study.

A major consequence of this statistical equivalence is that the spectral broadening observed in experiments around the Strouhal peak can be partially explained and modelled through a spanwise randomness of the vortex shedding phase.

6.4. Aeroacoustic implementation of the statistical model

Statistical pressure measurements on the rod surface provide the correlation coefficient $\rho(\eta)$. This can be related to a variance spanwise distribution $w(\eta) = -2\ln\{\rho(\eta)\}$. Then, $w(\eta)$ is used to generate a random phase sequence $\tilde{\varphi}(\eta_i, \tau_j)$ along the rod span.

Consistently with the observed vortex shedding behaviour, phase jumps are only permitted sporadically every two or three shedding cycles. Furthermore, jump synchronization at two different spanwise sections is avoided by slightly randomizing the time at which the phase jump occurs.

The random phase is then converted into a random perturbation of the retarded time by writing

$$\tilde{\tau}_{ret}(\eta, \tau) = \tau_{ret}(\eta, \tau) + \frac{\tilde{\varphi}(\eta, \tau_{ret}(\eta, \tau))}{2\pi\, St}, \tag{37}$$

where $\tau_{ret}(\eta, \tau)$ denotes the deterministic retarded time obtained from the dimensionless retarded time equation (3).

The aeroacoustic prediction can thus be performed by forcing into Eqs. (1) and (2) a spanwise random dispersion of the retarded time $\tilde{\tau}_{ret}(\eta, \tau)$. This is equivalent to introduce a loss of coherence into the spanwise repetition of the two-dimensional aerodynamic field.

Interestingly, the same two-dimensional aerodynamic field can be used to predict the acoustic pressure by using different seeds of the random phase distribution. Then, averaged acoustic spectra can be computed in a similar way as in the experiments.

7. Aerodynamic results

In Fig. 11, contours of the turbulent kinetic energy shows the vortical structures in the wake of the rod. These induce the aerodynamic force plotted in Fig. 12. The Strouhal frequency f_0 is about 293 Hz and the corresponding Strouhal number is 0.23, which slightly differs from the experimental value of 0.2. The unsteady lift exhibits odd harmonics ($f_0, 3f_0, \ldots$), whereas the unsteady drag exhibits even harmonics ($2f_0, 4f_0, \ldots$). This is because the vortices shed from either sides of the cylinder give the same contribution to the drag and opposite contributions to the lift. The amplitude of the fluctuating lift is $C_{l\,max} = 0.65$ which is greater than the experimental value of 0.5 [24,10]. This discrepancy can be partially explained by considering that the experimental
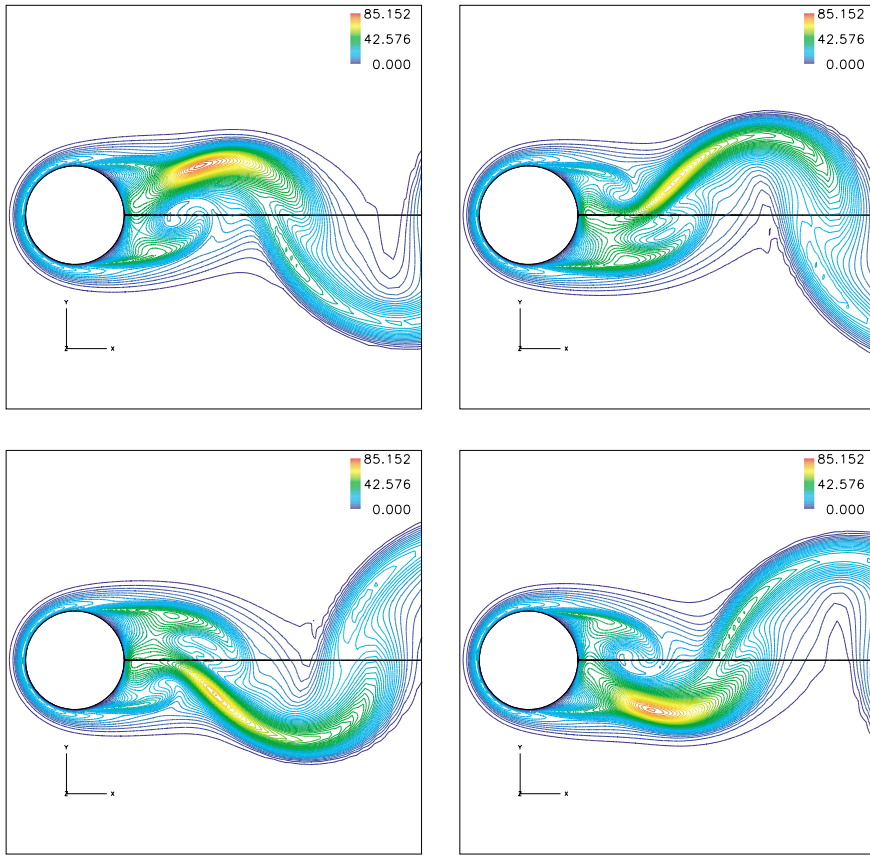
Fig. 11. Kinetic turbulent energy during a vortex shedding period. Snapshots clockwisely disposed.
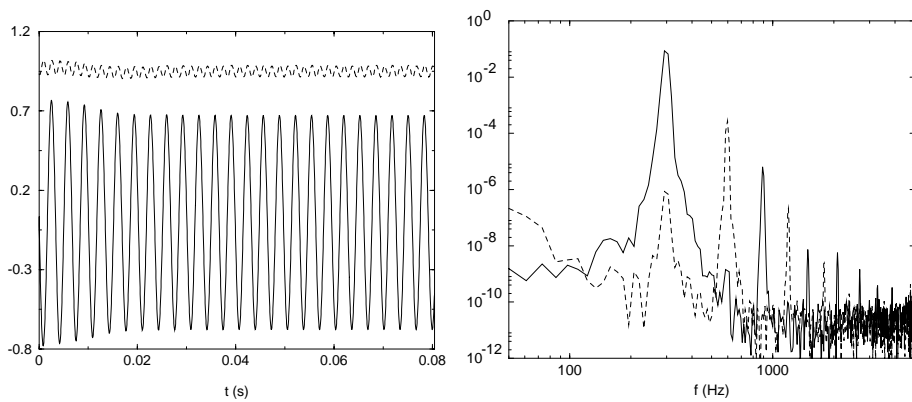
Fig. 12. Aerodynamic force on the cylinder: (——) C_l; (- - - -) C_d. Signals (left), spectra (right).
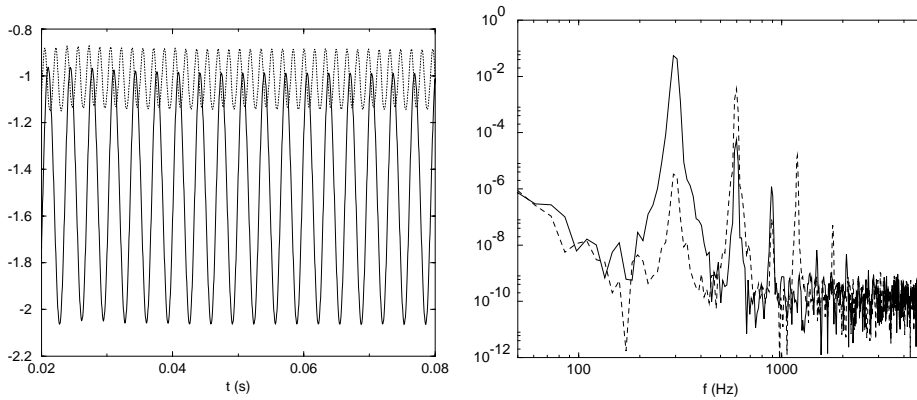
Fig. 13. Pressure coefficient on the cylinder surface. (——) $\phi = 90°$; (- - - -) $\phi = 0°$. Signals (left), spectra (right).

vortex shedding is not fully correlated along the rod span and thus results in smaller lift fluctuations. It is interesting to notice that the two-dimensional RANS prediction only features a deterministic flow unsteadiness, providing a periodic flow behaviour. The spectral broadening around the Strouhal frequency in Fig. 12(a) is indeed a by-product of the signals truncation, whose effects can be reduced by a data windowing, but not completely removed.

Fig. 13 shows the wall pressure coefficients at $\phi = 0°$ and $\phi = 90°$. A comparison between Figs. 12 and 13 shows that the wall pressure at the base point ($\phi = 0°$) and the drag have similar spectral behaviours. Analogously, the wall pressure at $\phi = 90°$ and the lift also do. This confirms Phillips' assumption of considering the wall pressure signal at $\phi = 90°$ as representative of the fluctuating lift. The base suction coefficient is $-C_{pB} = 1.01$ which is smaller than the experimental value of about 1.2 [21].

Counter-rotating vortices are shed from the cylinder at a Strouhal number $St = 0.23$. The overprediction of the vortex shedding frequency from a two-dimensional rod is a common CFD result [22] which can be explained to some extent. As argued by Roshko [23], the length of the mean recirculating region behind the rod results from a dynamic equilibrium between the base suction coefficient, the pressure distribution upon the recirculating bubble and the mean Reynolds stresses $\rho \overline{u'v'}$ in the separated flow region. Hence, higher Reynolds stresses correspond to shorter mean recirculating regions. In a 3-D flow a part of the energy extracted from the mean flow is used to maintain spanwise velocity fluctuations. As a consequence, the mean recirculating region extends farther from the cylinder and the Strouhal frequency is smaller than in a computed 2-D flow.

Letting $\langle \rangle$ denote the local average of a quantity over a vortex shedding period, the following quantities are plotted in Figs. 14 and 15:

- mean pressure coefficient, i.e.,

$$\langle Cp \rangle = \frac{\langle p - p_\infty \rangle}{\frac{1}{2}\rho_\infty V_\infty^2};\tag{38}$$
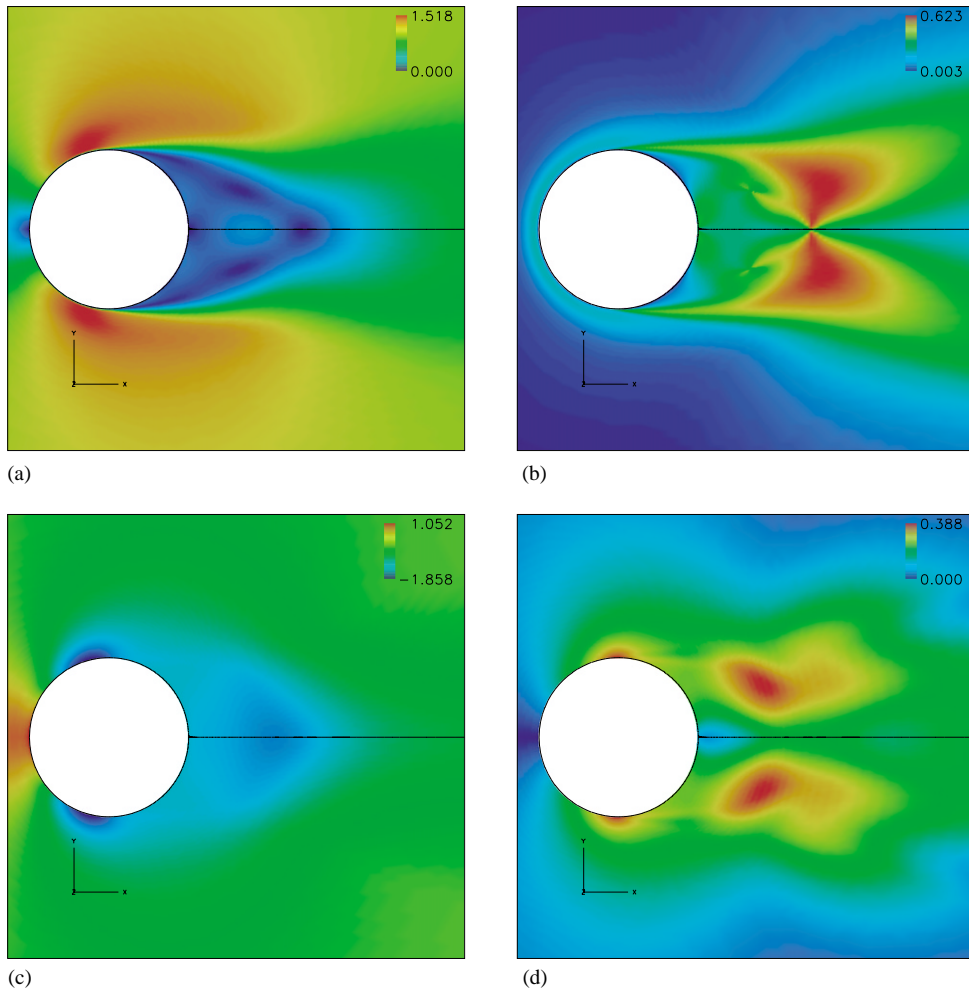
Fig. 14. Mean and fluctuating flow past the cylinder. (a) $\langle V \rangle$; (b) $V_{\text{r.m.s}}$; (c) $\langle Cp \rangle$; (d) $Cp_{\text{r.m.s}}$.

- root-mean-square pressure coefficient, i.e.,

$$Cp_{\text{r.m.s}} = \sqrt{\langle (Cp - \langle Cp \rangle)^2 \rangle}; \tag{39}$$

- dimensionless mean velocity, i.e.,

$$\langle V \rangle = \frac{\sqrt{\langle u \rangle^2 + \langle v \rangle^2}}{V_\infty}; \tag{40}$$

- dimensionless root-mean-square velocity, i.e.,

$$V_{r.m.s} = \sqrt{\langle (un_x/V_\infty + vn_y/V_\infty - \langle V \rangle)^2 \rangle + \tfrac{2}{3} \langle k \rangle}. \tag{41}$$
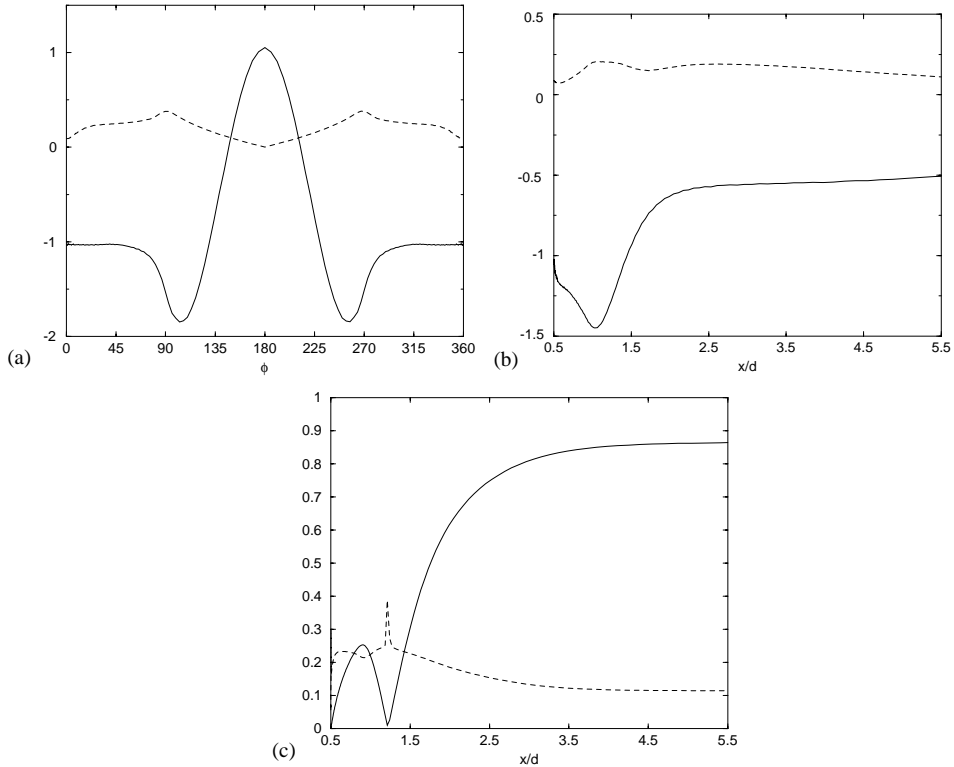
Fig. 15. Mean and fluctuating flow past the cylinder. (a) Wall pressure field: —— $\langle C_p \rangle$, - - - - $Cp_{\mathrm{r.m.s}}$; (b) pressure field in the wake of the rod ($y = 0$): —— $\langle Cp \rangle$, - - - - $Cp_{\mathrm{r.m.s}}$; (c) velocity field in the wake of the rod ($y = 0$): —— $\langle V \rangle$, - - - - $V_{\mathrm{r.m.s}}$.

Here $n_x = \langle u \rangle / \langle V \rangle$ and $n_y = \langle v \rangle / \langle V \rangle$ are the components of the mean flow direction and $\langle k \rangle$ denotes the mean turbulent kinetic energy.[3]

The mean velocity field in Figs. 14(a) and 15(c) highlights the recirculating region behind the rod. It can be observed that the downstream point of minimum $\langle V \rangle$ at ($x/d = 1.2, y = 0$) coincides with the point of maximum $V_{r.m.s.}$ (see Fig. 15(c)). Conventionally, such a point defines the *vortex formation length* l_F. Measurements made by Szepessy and Bearman [10] over a wide range of Reynolds numbers and rod aspect ratios show a vortex formation length of about $1.5d$. Thus, consistently with Roshko's [23] model, a two-dimensional computation provides a smaller mean recirculating region behind the rod.

Fig. 15(a) shows the pressure field on the rod surface. The $Cp_{r.m.s.}$ peaks at $\phi = 91°$, which marks the mean location of the separation point.

---

[3] Eq. (41) is based on the hypothesis of local isotropy of the turbulent velocity field, i.e., $k = \frac{3}{2}\overline{u'u'}$, where u' is the Reynolds fluctuating component of the velocity field in the x direction. Clearly, in the framework of unsteady RANS modelling, a fluctuating k only makes sense if the averaging time is longer than that associated with the slowest turbulent motions, but is much smaller than the time scale of the flow unsteadiness (the vortex shedding period in the present study).
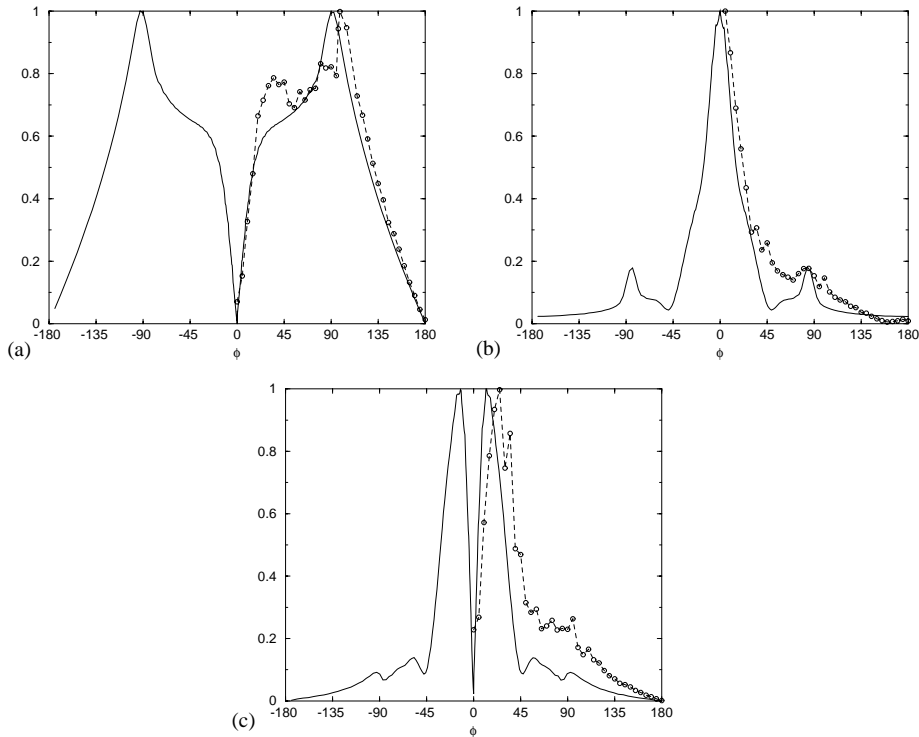
Fig. 16. Peaks of the normalized cross-spectrum amplitude $|S_{12}/\max(S_{12})|$ between a reference probe at $\phi = 90°$ and probes at different ϕ. (a) $f = f_0$; (b) $f = 2f_0$; (c) $f = 3f_0$. (∘) Experimental data; (——) RANS results.

In Fig. 16 the predicted Strouhal peak of the cross-spectrum between a wall pressure signal at $\phi = 90°$ and that at different ϕ around the cylinder is checked against the experimental data. Discrepancies in the separated flow region can be observed up to $\phi \simeq 50°$. Furthermore, as previously discussed, the measured cross-spectrum peaks at $\phi = 100°$.

The cross-spectra peak values at the first and second harmonics are plotted in Fig. 16(b) and (c), respectively. A fairly good agreement arises between experimental data and numerical predictions. Because of the major contribution given by the rod base point to the first harmonic ($2f_0$) fluctuations, the first harmonic peak of the cross-spectrum is maximum when the movable probe is at $\phi = 0°$. In addition, a local maximum occurs at the angular position $\phi = 85°$. At the second harmonic ($3f_0$) the computed cross-spectrum peaks when the movable probe is at $\phi = 12°$, whereas the experimental data exhibit a maximum at about $\phi = 25°$. Furthermore, both the numerical and the experimental cross-spectra exhibit a local maximum when the movable probe is at $\phi = 95°$.

Comparisons between numerical and experimental values of some representative quantities are summarized in Table 1.

8. Acoustic results

In this section acoustic results are presented and discussed. The three-dimensional flow necessary for the acoustic computation is recovered by a spanwise repetition of the computed

Table 1
Comparison between experimental data and RANS results

	Experimental	Numerical
St	0.2[a]	0.234
$C_{l\,max}$	0.5[a,c]	0.65
C_d	1.1[a]	0.95[d]
$-C_{pB}$	1.2[b]	1.01
l_F	1.5[c]	1.2

[a] Experimental data from Schewe [24].
[b] Experimental data from Williamson [21].
[c] Experimental data from Szepessy and Bearman [10].
[d] Experimental data from the predicted drag coefficient does not account for the viscous stresses.
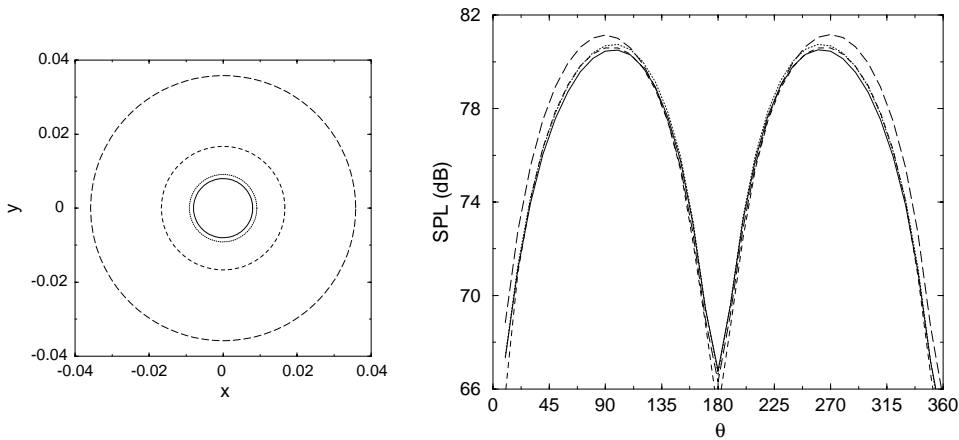
Fig. 17. Directivity pattern (right) obtained by integrating upon different surfaces (left) around the cylinder: (——) S1 (cylinder surface $r = 8 \times 10^{-3}$ m); (....) S2 ($r = 9.11 \times 10^{-3}$ m); (- -) S3 ($r = 1.67 \times 10^{-2}$ m); (— —) S4 ($r = 3.58 \times 10^{-2}$ m). 2-D computations.

two-dimensional flow. A deterministic repetition is referred to as 2-D, whereas, a randomly perturbed repetition is referred to as 3-D (spanwise statistical model). The wave propagation is of course three-dimensional, since the three-dimensional free space Green function is used in the FW–H integral formulation.

Firstly, the consistency of the no-quadrupole approximation is checked by comparing 2-D results obtained from different integration surfaces. Secondly, 2-D and 3-D results are checked against experimental data.

In Fig. 17(b) the sound directivities computed through Eqs. (1) and (2) applied to the surfaces in Fig. 17(a) are plotted. The agreement within 1 dB, which is fairly good, shows both the consistency of the penetrable surface FW–H formulation and the physical adequacy of neglecting the quadrupole contribution in the acoustic prediction.

The corresponding pressure signals computed at $\theta = 90°$ from the four integration surfaces are plotted in Fig. 18. The relative differences $\Delta p'/\max(|p'|)$ between the S1 results and those from S2 to S4 are plotted in Fig. 19. Significant discrepancies occur only for the outer surface S4 and are
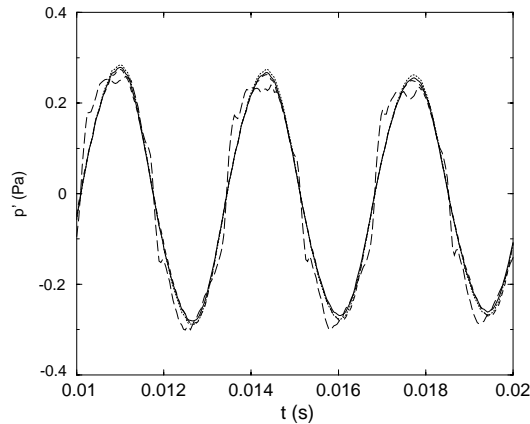
Fig. 18. Acoustic pressure signals computed from: (——) S1; (....) S2; (- -) S3; (— —) S4. 2-D computations at an observation angle $\theta = 90°$.
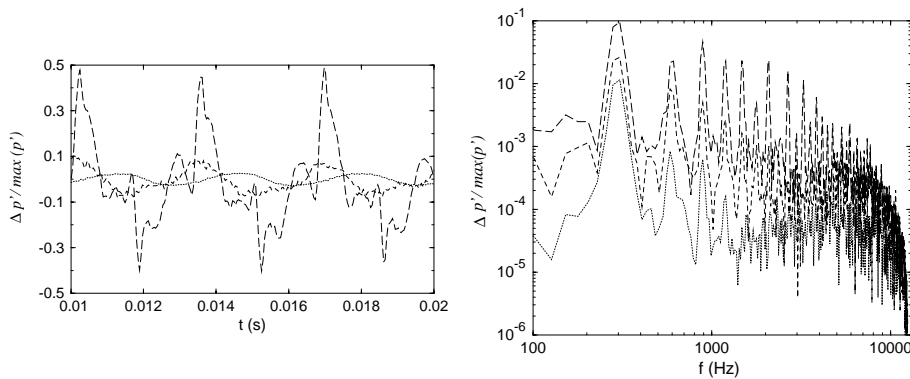
Fig. 19. Relative difference between S1 results and results from: (....) S2; (- -) S3; (— —) S4. 2-D computations at an observation angle $\theta = 90°$.

likely to be due to a degraded CFD accuracy far from the cylinder. The spectra of $\Delta p'/\max(|p'|)$ in Fig. 19(b) exhibit peaks at both even and odd harmonics. Although the reciprocal influence between physical and numerical effects on the observed discrepancies cannot be established without computing the volume contribution, these results confirm that the quadrupole contribution can be neglected in the present low Mach number aeroacoustic prediction.

In Figs. 20–22, 3-D computations are checked against 2-D computations and experimental measurements. A Gaussian correlation length of $5d$ is used in the spanwise statistical model. The computed acoustic spectra at each observation point are obtained by averaging over 100 spectra, each obtained with a different value of the random generation seed.

In Fig. 20 a comparison is shown between 2-D and 3-D acoustic signals. The random phase distribution along the rod span clearly results in a randomly amplitude modulation.

In Fig. 21, 2-D and 3-D computations are checked against experimental data. The measured power spectral density have been integrated upon frequency intervals of $\Delta f = 12$ Hz.
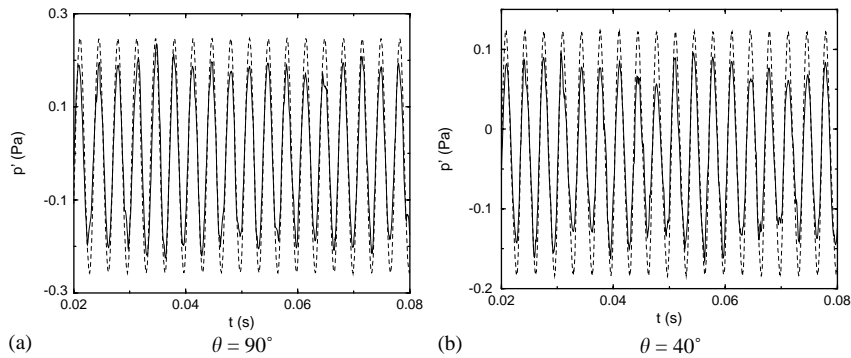
Fig. 20. Acoustic signals: (——) 2-D computation; (- - - -) 3-D computation.

Furthermore, in order to take into account the aerodynamic Strouhal frequency overprediction, the experimental data (f, dB) have been scaled to (f', dB'), i.e.,

$$f' = \frac{St_{num}}{St_{exp}} f, \quad dB' = dB + 20 \log\left(\frac{St_{num}}{St_{exp}}\right), \tag{42}$$

where the level correction accounts for the fact that the sound level is proportional to the vortex shedding frequency, as shown in Eq. (10).

As expected from a deterministic flow prediction, 2-D results only exhibit harmonic peaks without spectral broadening. On the contrary, forcing an ad hoc random behaviour permits to better fit the broadband noise levels. Moreover, the harmonic peaks are better predicted by 3-D computations.

At frequencies higher than about 3000 Hz the sound pressure level is underestimated. However, as previously pointed out, the experimental data are likely to be contaminated by the background noise which persists over a wider frequency range.

In Fig. 22 the 3-D prediction of the noise directivity is compared to the measured one. Numerical results have been obtained by adding the Fourier contributions in the overall frequency range, i.e., [12 Hz, 12.4 kHz], whereas the experimental values have been obtained by integrating the power spectral density upon the frequency range [100 Hz, 1000 Hz]. The agreement is good. Furthermore, a dipole-type $\sin \theta$ interpolation of the experimental data shows that the maximum radiation occurs at an observation angle slightly greater than $90°$. This is confirmed by the numerical prediction.

9. Conclusions

A hybrid *Aeolian tones* RANS/FW–H aeroacoustic prediction was performed at a Reynolds number of 2.2×10^4.

A deterministic periodic flow was predicted through a two-dimensional RANS approach. The Strouhal frequency was overestimated and the vortex formation length was underestimated. These
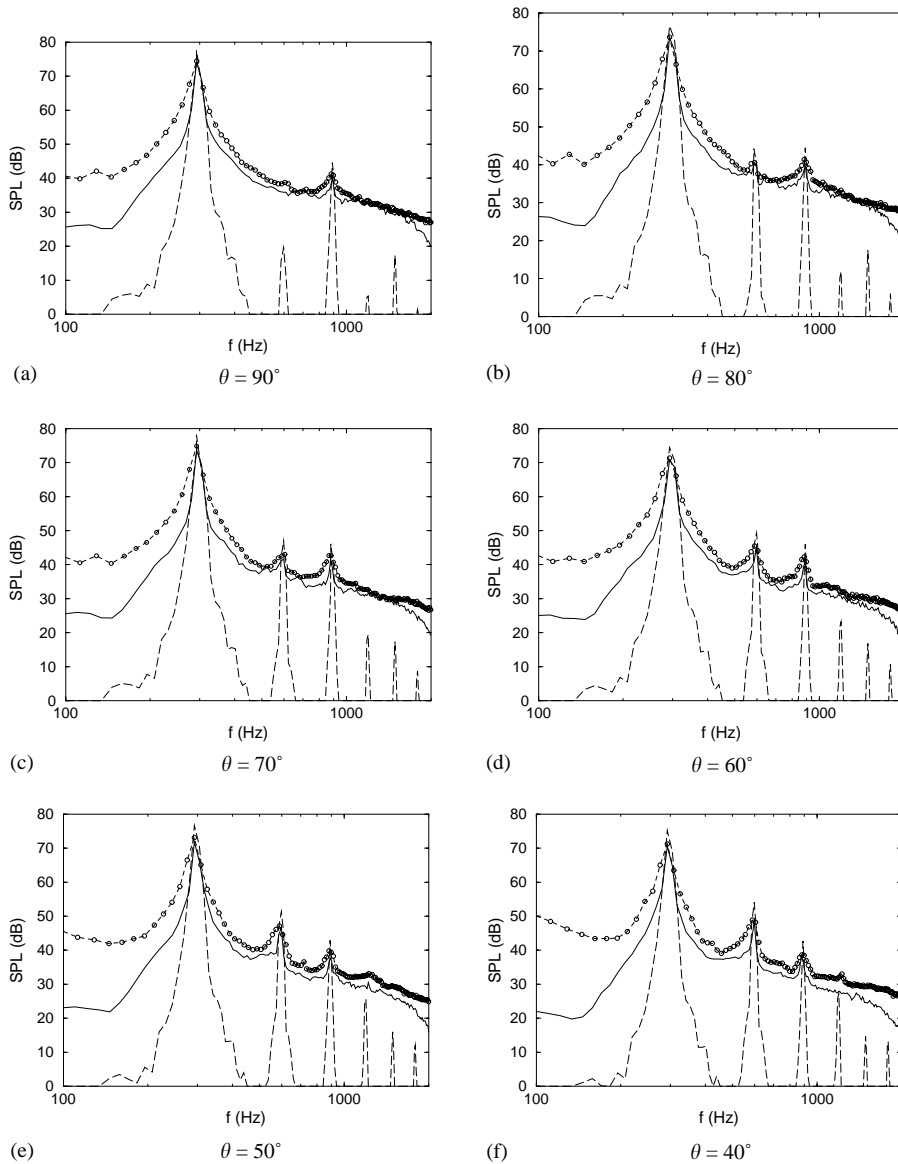
Fig. 21. Acoustic spectrum: (○) experimental data; (——) 3-D computation; (— —) 2-D computation.

results can be justified by invoking the fact that, in a two-dimensional computation, all the energy extracted from the mean flow is used to maintain in-plane fluctuations.

The application of the FW–H acoustic analogy to penetrable integration surfaces around the cylinder showed that the direct contribution of the detached eddies to the overall sound remains negligible, even though the lower end of the spectrum might be affected by surrounding broadband jet noise.
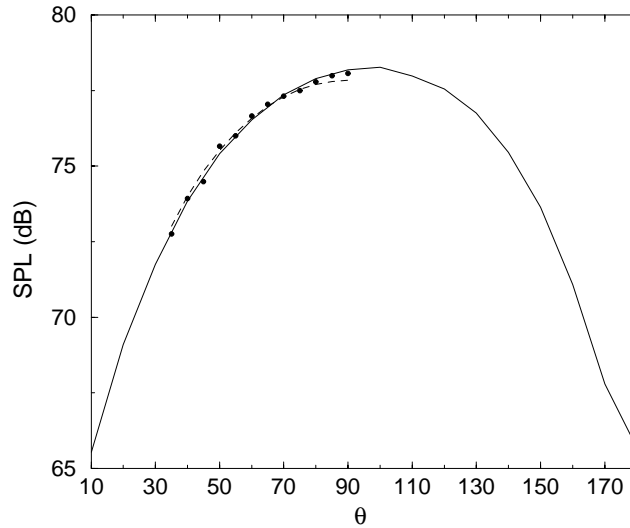
Fig. 22. Directivity pattern: (——) 3-D computation; (●●) experimental data; (— —) $K \sin \theta$ interpolation.

Acoustic results based on the spanwise repetition of the computed two-dimensional flow only featured the spectral harmonic peaks. Therefore, in order to partially recover the three-dimensional character of the flow, a statistical behaviour of the vortex shedding phase was forced into the spanwise repetition of the aerodynamic field. Phase lags were modelled on the basis of two-point statistical measurements and allowed the acoustic signals to undergo ad hoc amplitude modulations. As a consequence, the spectral broadening around the shedding frequency and its harmonics was quite well featured by merely performing a two-dimensional aerodynamic computation.

This type of approach is a promising tool wherever full three-dimensional flow computations are not affordable (as in turbomachines, for instance): two-dimensional unsteady RANS provides a deterministic unsteady flow to which the statistical model may be applied.

Appendix A. Coherence function and correlation coefficient

The coherence function Γ_{xy} between two signals $x(t)$ and $y(t)$ is defined as

$$\Gamma_{xy}(f) = \frac{|S_{xy}(f)|}{\sqrt{S_{xx}(f)S_{yy}(f)}}, \tag{A.1}$$

where $S_{xy}(f)$ is the cross-power spectral density $S_{xy}(f) = TF\{C_{xy}(\tau)\}$, with

$$C_{xy}(\tau) = \lim_{T \to \infty} \frac{1}{T} \int_0^T x(t)y(t-\tau)\,\mathrm{d}t \tag{A.2}$$

and *TF* denoting the Fourier transform. For an ergodic process $C_{xy}(\tau)$ can be interpreted as the correlation function between $x(t)$ and $y(t)$. The correlation coefficient ρ is defined as

$$\rho = \frac{C_{xy}(0)}{\sqrt{C_{xx}(0)C_{yy}(0)}} = \frac{\int_{-\infty}^{\infty} S_{xy}(f)\,\mathrm{d}f}{\sqrt{\int_{-\infty}^{\infty} S_{xx}(f)\,\mathrm{d}f}\sqrt{\int_{-\infty}^{\infty} S_{yy}(f)\,\mathrm{d}f}}. \tag{A.3}$$

In the case of two tuned monochromatic signals it results that $\rho = \Gamma_{xy}(f_0)$.

Appendix B. Symbols in the FW–H acoustic analogy

The aerodynamic field is introduced into Eqs. (1) and (2) in terms of conservative quantities: the flow density ρ, the linear momentum $\rho\tilde{u}_i$, $\tilde{u}_i$ being the relative velocity of the flow with respect to the integration surface $f = 0$, the specific total internal energy ρE and the specific kinetic turbulent energy ρk. A description of all the involved quantities is reported as follows:

$$p_d = \tfrac{1}{2}\rho_0 U_{ref}^2, \quad \theta = t U_{ref}/l_{ref}, \quad M_{ref} = U_{ref}/c,$$

$$V_i = v_i/U_{ref}, \quad V_n = V_i \hat{n}_i, \quad \tilde{u}_i = u_i - v_i,$$

$$\mathbf{X} = \mathbf{x}/l_{ref}, \quad \mathbf{Y} = \mathbf{y}/l_{ref},$$

$$\hat{r}_i = \frac{X_i - Y_i}{|\mathbf{X} - \mathbf{Y}|}, \quad R = |\mathbf{X} - \mathbf{Y}|,$$

$$M_i = v_i/c, \quad M_r = M_i \hat{r}_i, \quad \dot{M}_r = \dot{M}_i \hat{r}_i, \quad M_{or} = M_{oi}\hat{r}_i,$$

$$\sigma = \frac{\rho}{\rho_0}, \quad q_i = \frac{(\rho\tilde{u}_i)}{(\rho_0 U_{ref})}, \quad e = \frac{(\rho E)}{(\rho_0 U_{ref}^2)}, \quad k = \frac{(\rho K)}{(\rho_0 U_{ref}^2)},$$

$$C_p = 2\left\{(\gamma - 1)\left[e - \frac{q_i q_i}{2\sigma} - k\right] - \frac{p_0}{2p_d}\right\},$$

$$\dot{C}_p = 2(\gamma - 1)\left[\dot{e} - \frac{q_i \dot{q}_i}{\sigma} + \dot{\sigma}\frac{q_i q_i}{2\sigma^2} - \dot{k}\right],$$

$$\lambda_i = \frac{C_p}{2}\hat{n}_i + V_i q_n + \frac{q_i q_n}{\sigma},$$

$$\chi_i = \frac{\dot{C}_p}{2}\hat{n}_i + \frac{C_p}{2}\dot{\hat{n}}_i + \dot{V}_i q_n + V_i(\dot{q}_i \hat{n}_i) + V_i(q_i \dot{\hat{n}}_i) + \frac{\dot{q}_i q_n}{\sigma} + \frac{q_i(\dot{q}_i \hat{n}_i)}{\sigma} + \frac{q_i(q_i \dot{\hat{n}}_i)}{\sigma} - \frac{q_i q_n}{\sigma^2}\dot{\sigma},$$

$$q_n = q_i \hat{n}_i, \quad \lambda_M = \lambda_i M_i, \quad \lambda_r = \lambda_i \hat{r}_i, \quad \chi_r = \chi_i \hat{r}_i.$$

In the above expressions p_0 and ρ_0 are the quiescent fluid pressure and density, respectively, $\mathbf{M}_o$ denotes the observer Mach number, $\hat{n}_i$ is the unit vector pointing out of the integration surface and upper dots denote derivatives with respect to the dimensionless time θ. The loading-noise term χ_i is the dimensionless time derivative of λ_i.

Other details concerning the rotor noise code *Advantia* and the implemented FW–H formulation can be found in Refs. [19,25].

References

[1] V. Strouhal, Ueber eine besondere art der tonerregung, Annalen der Physik und Chemie (Leipzig) 3 (5) (1878) 216–251.

[2] J.W.S. Rayleigh, Acoustical observations II, Philosophical Magazine 7 (1879) 149–162.

[3] J.W.S. Rayleigh, Aeolian tones, Philosophical Magazine 29 (1915) 434–444.

[4] P.E. Doak, Analysis of internally generated sound in continuous materials: 2. A critical review of the conceptual adequacy and physical scope of existing theories of aerodynamic noise, with special reference to supersonic jet noise, Journal of Sound and Vibrations 25 (2) (1972) 263–335.

[5] J.W.S. Rayleigh, The Theory of Sound, Vols. I and II. Macmillan, London, 1896.

[6] M.J. Lighthill, On sound generated aerodynamically: 1. General theory, Proceedings of the Royal Society A 211 (1952) 564–578.

[7] N. Curle, The influence of solid boundaries upon aerodynamic sound, Proceedings of the Royal Society A 231 (1955) 505–514.

[8] O.M. Phillips, The intensity of aeolian tones, Journal of Fluid Mechanics 1 (1956) 607–624.

[9] C.H.K. Williamson, Oblique and parallel modes of vortex shedding in the wake of a circular cylinder at low Reynolds numbers, Journal of Fluid Mechanics 206 (1989) 579–627.

[10] S. Szepessy, P.W. Bearman, Aspect ratio and end plate effects on vortex shedding from a circular cylinder, Journal of Fluid Mechanics 234 (1992) 191–217.

[11] K.S. Brentner, A superior Kirchhoff method for aeroacoustic noise prediction: the Ffowcs Williams–Hawkings equation, 134th Meeting of the Acoustical Society of America, 1997.

[12] J.S. Cox, C.L. Rumsey, K.S. Brentner, Computation of sound generated by viscous flow over a circular cylinder, NASA Technical Memorandum 110339, 1997.

[13] K.S. Brentner, F. Farassat, An analytical comparison of the acoustic analogy and Kirchhoff formulation for moving surfaces, American Helicopter Society 53rd Annual Forum, 1997.

[14] D.J. Tritton, Experiments on the flow past a circular cylinder at low Reynolds numbers, Journal of Fluid Mechanics 45 (1959) 203.

[15] M. König, H. Heisenlohr, H. Eckelmann, Visualisation of the spanwise cellular structure of the laminar wake of wall-bounded circular cylinders, Physics of Fluids A 4 (1992) 869.

[16] M. Roger, S. Pérennès, Low-frequency noise sources in two-dimensional high-lift devices, American Institute of Aeronautics and Astronautics Paper 2000-1972, 2000.

[17] P. Ferrand, S. Aubert, L. Smati, O. Bron, H.M. Atassi, Nonlinear interaction of upstream propagating sound with unsteady transonic flow in a nozzle, American Institute of Aeronautics and Astronautics Paper 98-2213, 1998.

[18] D.C. Wilcox, Comparison of two equations turbulence models for boundary layers with pressure gradient, American Institute of Aeronautics and Astronautics Journal 31 (8) (1993) 1414–1421.

[19] D. Casalino, An advanced time approach for acoustic analogy prediction, Journal of Sound and Vibration 261 (4) (2003) 583–612.

[20] K.S. Brentner, F. Farassat, An analytical comparison of the acoustic analogy and Kirchhoff formulation for moving surfaces, American Institute of Aeronautics and Astronautics Journal 36 (8) (1998) 1379–1386.

[21] C.H.K. Williamson, Vortex dynamics in the cylinder wake, Annual Review of Fluid Mechanics 28 (1996) 477–539.

[22] C. Kato, M. Ikegawa, Large eddy simulation of unsteady turbulent wake of a circular cylinder using the finite element method, Advances in Numerical Simulation of Turbulent Flows, American Society of Mechanical Engineers, FED 117 (1991) 117.

D. Casalino, M. Jacob / Journal of Sound and Vibration 262 (2003) 815–844

[23] A. Roshko, Perspectives on bluff body aerodynamics, Journal of Wind and Industrial Aerodynamics 49 (1–3) (1993) 79–100.
[24] G. Schewe, On the force fluctuations acting on a cylinder in crossflow from subcritical up to transcritical Reynolds numbers, Journal of Fluid Mechanics 133 (1983) 265–285.
[25] D. Casalino, Analytical and Numerical Methods in Vortex-Body Aeroacoustics, Ph.D. Thesis, Politecnico di Torino and Ecole Centrale de Lyon, 2002.